Defect Structure of Localized Excitons in a WSe$_2$ Monolayer

Shuai Zhang,[1] Chen-Guang Wang,[2] Ming-Yang Li,[3,4] Di Huang,[1] Lain-Jong Li,[4] Wei Ji,[2,*] and Shiwei Wu[1,5,†]

[1]*State Key Laboratory of Surface Physics, Key Laboratory of Micro and Nano Photonic Structures (MOE),
and Department of Physics, Fudan University, Shanghai 200433, China*
[2]*Department of Physics and Beijing Key Laboratory of Optoelectronic Functional Materials and Micro-Nano Devices,
Renmin University of China, Beijing 100872, China*
[3]*Research Center for Applied Sciences, Academia Sinica, Taipei 10617, Taiwan*
[4]*Physical Sciences and Engineering Division, King Abdullah University of Science and Technology,
Thuwal 23955-6900, Saudi Arabia*
[5]*Collaborative Innovation Center of Advanced Microstructures, Nanjing 210093, China*
(Received 25 February 2017; revised manuscript received 23 May 2017; published 25 July 2017)

The atomic and electronic structure of intrinsic defects in a WSe$_2$ monolayer grown on graphite was revealed by low temperature scanning tunneling microscopy and spectroscopy. Instead of chalcogen vacancies that prevail in other transition metal dichalcogenide materials, intrinsic defects in WSe$_2$ arise surprisingly from single tungsten vacancies, leading to the hole (p-type) doping. Furthermore, we found these defects to dominate the excitonic emission of the WSe$_2$ monolayer at low temperature. Our work provided the first atomic-scale understanding of defect excitons and paved the way toward deciphering the defect structure of single quantum emitters previously discovered in the WSe$_2$ monolayer.

Direct-gap semiconducting transition metal dichalcogenide (TMD) monolayers in the form of MX_2 ($M =$ Mo, W; $X =$ S, Se) have spurred great interests for electronics, optoelectronics, and valleytronics [1,2]. However, typical TMD-based field effect transistor devices show n- or p-type behavior without intentional doping [3,4], contradicting what one would expect from a perfect crystal structure. Meanwhile, the carrier mobilities are also far below theoretical predictions [3,5]. Furthermore, the photoluminescence spectra not only show a strong excitonic effect, but also ensue a broad defect-activated emission peak within the optical band gap [1,2]. In addition, the photoluminescence quantum yield is unexpectedly low for a direct-gap semiconductor [6]. All these facts suggest that structural defects in TMD monolayers play significant roles in the electronic and optical properties [7–9].

Among the family of semiconducting TMD monolayers, defects in the WSe$_2$ monolayer exhibit some peculiar behavior. Because transition metal atoms are sandwiched between chalcogen atoms, the latter are believed to be easily removed, and chalcogen vacancies are often regarded as the most common intrinsic defect [10–13]. Accordingly, most TMD monolayers are n-type doped [3,14]. However, the WSe$_2$ monolayer usually shows p-type doping, either by mechanical exfoliation or chemical vapor deposition (CVD) [4,15]. This p-type doping provides a natural route to fabricating a p-n junction based on lateral heterostructure [14,16]. Moreover, in conjunction with giant spin-orbit splitting and spin-valley locking at the valence band, p-type doping facilitates the manipulation of valley coherence for a more extended time to 1–10 ns [17,18], in comparison to $\sim$10 ps with n-type doping [19]. More interestingly, when

the WSe$_2$ monolayer is cooled below $\sim$10 K, the defect-related localized exciton emissions behave as single quantum emitters (SQEs) [20–23], which are essential for quantum information processing [9]. Nevertheless, very little is known about the atomic and electronic structures of the defects in the WSe$_2$ monolayer. Here we used the low temperature scanning tunneling microscopy (STM) and spectroscopy (STS) to noninvasively probe the defect structure in a CVD grown WSe$_2$ monolayer at 16 K. We surprisingly found that intrinsic defects in the WSe$_2$ monolayer arise from single tungsten vacancies, instead of chalcogen vacancies that prevail in other TMD materials. The tungsten vacancy is the cause of hole (p-type) doping and dominated the emission of localized excitons at low temperature. With this finding, the above-mentioned peculiar behaviors in the WSe$_2$ monolayer could be mostly understood.

The WSe$_2$ monolayer sample was directly grown on highly oriented pyrolytic graphite (HOPG) by CVD [15]. The experiments of sample growth, STM and STS, photoluminescence or Raman, and density functional theory (DFT) calculations are shown in the Supplemental Material [24]. Figure 1(a) shows a STM topographic image of the WSe$_2$ monolayer at the bias voltage of -2.5 V. Identical pitlike atomic structures were randomly distributed in the WSe$_2$ monolayer. Given the high defect density, the possibility of impurity defects or defects in HOPG is unlikely (Fig. S1), and such structures are due to intrinsic defects. When the same area was imaged at a different bias voltage (-1.5 V), these pitlike structures exhibited as trefoil-like ones [Fig. 1(b)]. The sharp contrast illustrated a drastic difference between electronic structure of defects and that of the pristine monolayer. Such a difference could
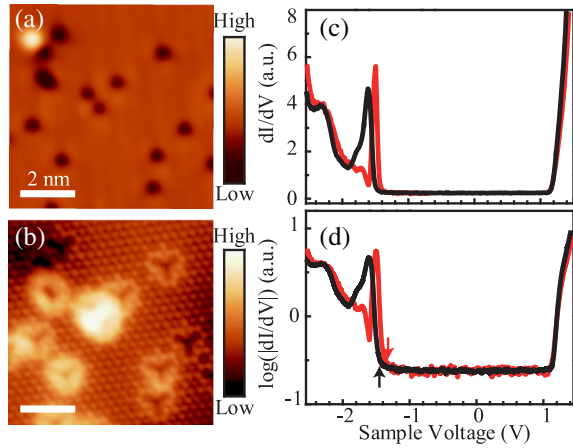
FIG. 1. STM topographic images and dI/dV spectrum of the WSe$_2$ monolayer grown on HOPG by CVD. (a),(b) STM images showing individual point defects in the WSe$_2$ monolayer for the same area but with different bias voltages of -2.5 and -1.5 V, respectively. $I_{set} = 100$ pA. The pitlike and trefoil-like structures in the images reflect the electronic distribution at different energy. (c),(d) Linear and logarithm plots of a typical dI/dV spectrum acquired on defect-free monolayer area (black curves) and on the defect site (red curves), respectively. $V_b = -2.5$ V, $I_{set} = 100$ pA. The edges (onsets) of the valence band at negative bias voltage were marked by arrows.
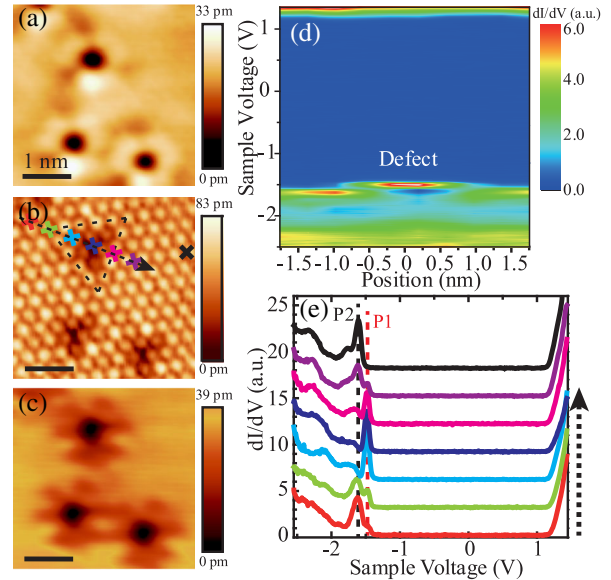

FIG. 2. Atomically resolved STM imaging and spectroscopy of individual point defects. (a),(b),(c) Close-up STM topographic images showing three identical point defects at different bias voltages of -1.8, -1.2, and $+1.5$ V, respectively. When the bias voltage was set within the semiconducting band gap, the outmost selenium atoms in the WSe$_2$ monolayer exhibited as individual protrusions in (b). The point defects were centered on the tungsten atom sites, preserving the trigonal symmetry in the WSe$_2$ monolayer. (d) 2D plot of dI/dV spectra along a line across the defect shown in (b). (e) A few dI/dV spectra selected from (d). The corresponding positions were also marked as crosses in (b). All the spectra are shifted vertically for clarity. For comparison, a dI/dV spectrum away from defects is also shown in the black curve. The peak shifts near the valence band edge (at negative bias voltage) were marked by two vertical dashed lines as P_1 (-1.48 V, red) and P_2 (-1.61 V, black), respectively.

be directly captured in the STS measurements on and off the defects. Figures 1(c) and 1(d) show typical dI/dV spectra on an isolated defect and a defect-free pristine area in both linear and logarithmic plots. On the defect-free pristine monolayer, the dI/dV spectra showed a wide quasiparticle band gap of 2.57 eV. The conduction band edge was slightly closer to the zero bias voltage, determined by band alignment with the graphite substrate. The band gap of 2.57 eV is also consistent with previous STS measurement on a WSe$_2$ monolayer grown on graphite by molecular beam epitaxy (MBE) [31]. We were also aware that the band gap value is slightly larger than that reported in Ref. [32], in which the sample was prepared by mechanical exfoliation and dry transfer techniques. Different strain and coupling with the substrate likely cause the discrepancy on band gap value. In contrast, the dI/dV spectra on the isolated defect revealed a different density of states distribution with a reduced band gap of 2.48 eV. This band gap narrowing of ~ 90 meV occurred near the edge of the valence band, corresponding to the onset shift at negative bias voltage in dI/dV spectra. Meanwhile, the dI/dV profiles near the conduction band remained identical. The up-shift of the valence band edge strongly suggests that these types of intrinsic defects act as p-type doping sites to the WSe$_2$ monolayer.

To further reveal the atomic structure of defects, we focused on individual defects by performing close-up STM measurements. Figures 2(a)–2(c) show STM topographic images of the same area at different bias voltages. Three individual defects were observed, which showed different

electronic distribution with respect to the bias voltage. Particularly when the bias voltage was set inside the semiconducting band gap, an atomically resolved STM topographic image was obtained, as illustrated in Fig. 2(b). If the tip-sample distance was closer by setting a smaller bias voltage, the moiré pattern formed between the WSe$_2$ monolayer and underlying graphite surface could also be imaged (Fig. S2). Individual protrusions in Fig. 2(b) were sitting in a triangular lattice with a distance of 3.3 Å, which is exactly equal to the nearest interatomic spacing (Se-Se or W-W) in the WSe$_2$ monolayer [33]. Because tungsten atoms are sandwiched between selenium atoms in the WSe$_2$ monolayer, these individual protrusions directly correspond to selenium atoms. This assignment is also consistent with previous STM topographic images on TMD monolayers such as MoSe$_2$ [34,35], and is further confirmed by recent atomically resolved atomic force microscopy (AFM) and STM [36]. By closely examining the atomically resolved images, the defects were centered on the tungsten sites, instead of selenium sites. Around the defects, neighboring selenium atoms appeared to be
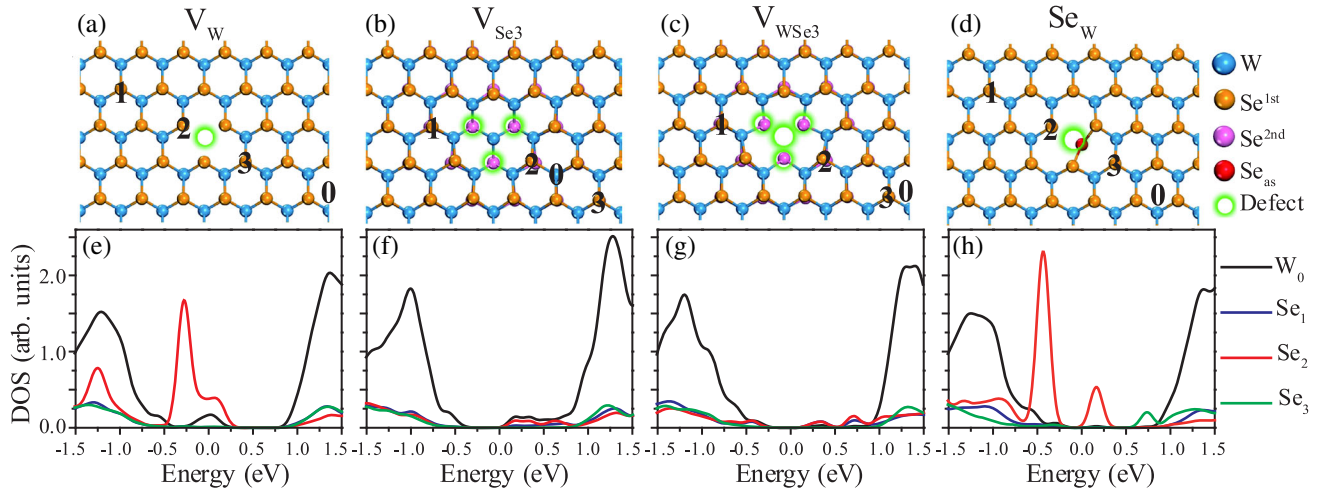
FIG. 3. Calculated atomic structures and corresponding LDOS of four defect structures. (a)–(d) Top view of the fully relaxed atomic structures of the energetically most favorable configurations for single V_W, V_{Se3}, V_{WSe3}, and Se_W defects, respectively. Solid blue, orange, pink, and red balls and the hollow green ball represent the W, Se atoms in the first sublayer, Se atoms in the second sublayer, the Se antisite atom, and original sites for the removed atoms, respectively. (e)–(h) Corresponding LDOS of the defects above. Black (W_0), blue (Se_1), red (Se_2), and green (Se_3) curves correspond to LDOS on the W atoms and Se atoms as marked in (a)–(d), respectively. In the calculations, the vacuum level was aligned with that of multilayer graphene, and the charge neutral point of the aligned graphene was thus chosen as the Fermi level in these LDOSs.

slightly lower than other selenium atoms in the defect-free area. Furthermore, the spatial distribution of electronic states around the defect exhibited trigonal symmetry centered around a tungsten site. Therefore, we could exclude defect structures centered on selenium sites such as a single selenium vacancy, despite that it was often thought to prevail in TMD monolayers [10–13].

Now we discuss the spatial dependent electronic structure of this intrinsic defect. Figure 2(d) shows a 2D plot of dI/dV spectra as a function of bias voltage and position along the dashed line cutting through the center of a defect. Consistent with that in Fig. 1(c), the defect significantly renormalized the valence band edge, which shifted toward the Fermi level in the vicinity of the defect, and reduced the quasiparticle band gap by about 90 meV. Furthermore, this shift in the valence band edge extended to about 1.5 nm around the defect. For a detailed examination on spectroscopic features, Fig. 2(e) shows a few selected dI/dV spectra along the dashed black line in Fig. 2(b). Near the defect, a new state (denoted as P_1) appears at the edge of the valence band. Meanwhile, the original peak (denoted as P_2) at the valence band in the defect-free area diminished when the intensity of P_1 became more intense, suggesting the competition between these two states. Such competition is well reflected in the STM images in Figs. 1(a) and 2(a), in which the bias voltages were set close to P_1 and P_2, respectively.

Knowing that the intrinsic defects are centered on the tungsten (W) sites instead of selenium (Se) sites, we proposed four possible defect structures including the single W vacancy (V_W), the vacancy complex of three Se atoms (V_{Se3}), the vacancy complex of W and three neighboring Se (V_{WSe3}), and the antisite defect where a Se substitutes a W atom (Se_W). Figures 3(a)–3(d) show the fully relaxed atomic structures

of these four candidates, respectively, revealed with DFT calculation. After structural relaxation, the V_W, V_{Se3}, and V_{WSe3} kept their trigonal symmetry. However, trigonal symmetry of the antisite defect (Se_W) is broken, which does not agree with our STM result and can be ruled out. The remaining three candidates are the single W vacancy and vacancy complex involving neighboring Se atoms. Furthermore, we calculated the local density of states (LDOS) for the above defect structures in Figs. 3(e)–3(h), along with the pristine WSe_2 monolayer and single selenium vacancy (V_{Se}) defect structure in Fig. S3. Although the DFT calculations underestimated the actual (experimental) values, it reveals that W vacancy causes an electron deficiency locally, and leads to p-type doping in the WSe_2 monolayer. Conversely, a chalcogen vacancy or vacancy complex leads to n-type doping, which modifies the local electronic structure near the conduction band. These results are consistent with the general rules of doping effects in semiconductors. Thus, the p-type doping revealed by STS suggests that the defect structure in our CVD grown WSe_2 monolayer sample is the single W vacancy (V_W). It is interesting to remark that the single W vacancy is not the most favored defect structure from our formation enthalpy calculations (Fig. S4). Rather, a single selenium vacancy has the lowest formation enthalpy as that in other TMD materials [10–13]. On the other hand, it is known that crystal growth is a dynamic and nonequilibrium process, not always determined by energetics (for example, line defects in a CVD grown MoS_2 monolayer on sapphire) [37]. The surprising finding of a single tungsten vacancy in the WSe_2 monolayer illustrates the importance of experimental characterization on defect structures.

With the atomic and electronic structures of the defect identified, we can now understand how they affect the optical
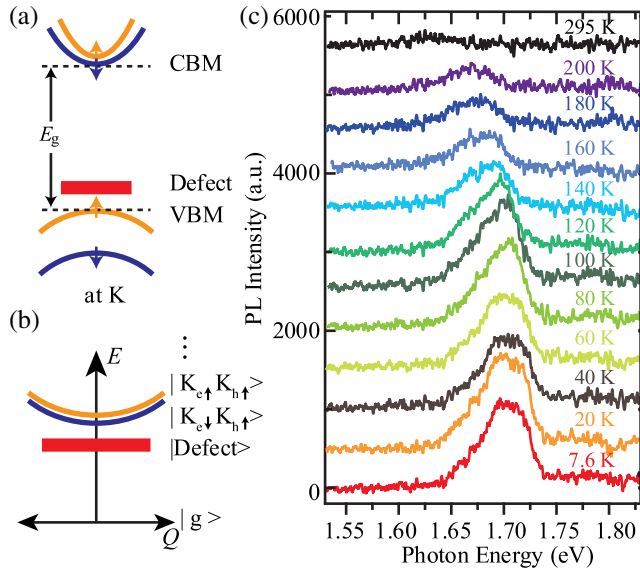
FIG. 4. Localized exciton arising from tungsten vacancy defects. (a),(b) Electronic and excitonic schematic diagrams of the WSe$_2$ monolayer, respectively. For the sake of simplicity, only the band structure at the K point is drawn. The spin configuration at the K' point is inverted because of time reversal symmetry, but would not affect the energy alignment of bright $|K_{e\uparrow}K_{h\uparrow}\rangle$ and dark $|K_{e\downarrow}K_{h\uparrow}\rangle$ free excitons as discussed in the text. (c) Temperature-dependent photoluminescence spectra of the WSe$_2$ monolayer on graphite. The data were obtained from the same location on the sample, and spectra are offset for clarity. The excitation wavelength and power were 532 nm and 1.60 mW, respectively.

properties of the WSe$_2$ monolayer. As illustrated in Fig. 4(a), both the conduction and valence bands at the K point of TMDs are spin polarized due to the spin-orbit splitting (tens of meV for conduction band and hundreds of meV for valence band). For the WSe$_2$ monolayer, the minimum gap occurs between bands of opposite electron spin, giving rise to the optically forbidden (dark) free exciton lying $\sim$30 meV below the bright free exciton [Fig. 4(b)] [30]. Thus, the bright free exciton emission could be thermally activated at room temperature, and its intensity would drop at lower temperature. Figure 4(c) shows the photoluminescence spectra at variable temperature from the sample. Overall, the photoluminescence from WSe$_2$ monolayer on graphite was heavily quenched, so that the intensity was about 5 orders of magnitude weaker than that from WSe$_2$ monolayer on oxidized silicon wafer (Fig. S5). At low temperature $\sim$7 K, the photoluminescence spectra were dominated by a broad peak centered around 1.70 eV, very close to the energy of free excitons in WSe$_2$ monolayer. However, the photoluminescence intensity increases at the lower temperature, which is opposite to that expected for free excitons as discussed above. The broad peak profile also excluded the possibility of free charged exciton (trions). In contrast, the localized defect excitons could emit brightly at low temperature, because the energies of spin-split defect states are nearly degenerate as suggested from the spin-resolved band
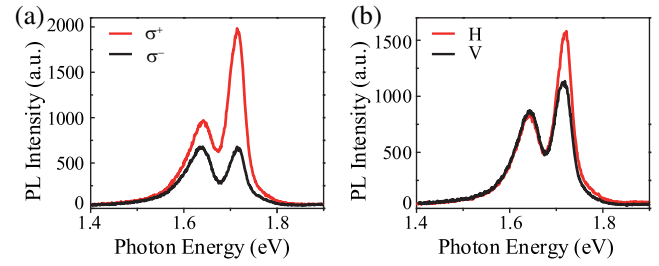

FIG. 5. Valley polarization and valley coherence of the CVD-grown WSe$_2$ monolayer on sapphire. (a) Polarization-resolved photoluminescent spectra for σ^+ detection under circularly polarized excitation of laser at 1.96 eV and 26 K. The red and black lines correspond to σ^+ and σ^- excitation, respectively. The circular polarization of the free exciton (1.72 eV) and the defect exciton (1.64 eV) was 49% and 16%, respectively. (b) Polarization-resolved photoluminescence spectra for horizontally polarized (H) detection under the linearly polarized excitation of laser at 1.96 eV and 26 K. The red and black lines correspond to the horizontally (H) and vertically (V) polarized excitation, respectively. The valley coherence was only observed on the free exciton.

structure calculation on the single tungsten vacancy defect (Fig. S6). Meanwhile, the point defect wave function has a spatial extension of $\sim$1.5 nm, very close to the free exciton radius of $\sim$1 nm [34]. Therefore, the defect exciton would have similar binding energy to that of free excitons, and down-shift its energy almost proportional to the quasiparticle band gap reduction ($\sim$90 meV). Hence, the energy of defect excitons is only slightly lower than that of free excitons, which is consistent with the low temperature photoluminescence spectra.

The energy of defect excitons also matches well with that from SQEs observed in the WSe$_2$ monolayer, suggesting the tungsten vacancy defect to be a candidate of such emitters [20–23]. According to previous studies, the SQEs are subject to the circularly polarized optical selection rule, especially under high magnetic field. Such circular dichroism on SQEs indicates the trigonal symmetry for their atomic structures, much as the pristine semiconducting TMD monolayers for valley selectivity [1,2]. To this end, we measured the circularly polarized photoluminescence spectra from the WSe$_2$ monolayer on sapphire, which was grown with the same method as that on graphite. Now, without the strong quenching from graphite, both free excitons and defect excitons clearly appeared in the low temperature photoluminescence spectra in Fig. 5. They both exhibited circular dichroism when the sample was excited by σ^+ or σ^- circularly polarized light. The circular polarization of the free exciton (49% at 1.72 eV) is larger than that of the defect exciton (16% at 1.64 eV). Furthermore, the linear polarization was only observed on the free exciton, which suggests the absence of valley coherence on the defect exciton [38]. All these data proved that the trigonal symmetry of the single tungsten vacancy defect was somewhat reduced, but still preserved. The perturbation likely came from the moiré pattern formed between the WSe$_2$ monolayer and graphite

substrate. We expect that the degree of circular polarization would further increase if a strong magnetic field is applied. Occasionally, we also observed the coupling between defects when they are very close, as exemplified in Fig. S7 [24]. The spatial overlapping of their electronic wave functions completely destroyed the trigonal symmetry of individual defects. Thus, the circular dichroism would not be expected for coupled defects, even under high magnetic field. Based on these observation and analysis, we reasonably conjecture that the tungsten vacancy defect is a likely candidate, at least a precursor, for SQEs in the WSe_2 monolayer. Unfortunately, we did not observe the emergence of individual sharp peaks at temperature below ~10 K, another key signature of SQEs. We attribute this absence to the high density of defects in our CVD-grown sample, which caused inhomogeneous broadening on the emission spectra [20].

In summary, we used low temperature STM and STS to study the atomic and electronic structures of intrinsic defects in WSe_2 monolayer. In corroboration with *ab initio* calculations, we unveiled the individual point defects to be single tungsten vacancy with trigonal symmetry, which is responsible for the *p* doping of the WSe_2 monolayer. We further discovered on the same sample that these vacancy defects dominated the low temperature optical spectra as localized excitons. For the first time, our work shed light on the atomic-scale defect structure of localized excitons in the WSe_2 monolayer and paved the way toward defect engineering for SQEs in TMD monolayers and other 2D materials in general [7–9].

---

[*]Corresponding author.
wji@ruc.edu.cn
[†]Corresponding author.
swwu@fudan.edu.cn

[1] X. Xu, W. Yao, D. Xiao, and T. F. Heinz, Nat. Phys. **10**, 343 (2014).

[2] J. R. Schaibley et al., Nat. Rev. Mater. **1**, 16055 (2016).

[3] B. Radisavljevic, A. Radenovic, J. Brivio, V. Giacometti, and A. Kis, Nat. Nanotechnol. **6**, 147 (2011).

[4] H. Fang, S. Chuang, T. C. Chang, K. Takei, T. Takahashi, and A. Javey, Nano Lett. **12**, 3788 (2012).

[5] K. Kaasbjerg, K. S. Thygesen, and K. W. Jacobsen, Phys. Rev. B **85**, 115317 (2012).

[6] M. Amani et al., Science **350**, 1065 (2015).

[7] O. V. Yazyev and Y. P. Chen, Nat. Nanotechnol. **9**, 755 (2014).

[8] Z. Lin, B. R. Carvalho, E. Kahn, R. Lv, R. Rao, H. Terrones, M. A. Pimenta, and M. Terrones, 2D Mater. **3**, 022002 (2016).

[9] I. Aharonovich, D. Englund, and M. Toth, Nat. Photonics **10**, 631 (2016).

[10] Y. Lin et al., Nat. Commun. **6**, 6736 (2015).

[11] W. Zhou, X. Zou, S. Najmaei, Z. Liu, Y. Shi, J. Kong, J. Lou, P. M. Ajayan, B. I. Yakobson, and J.-C. Idrobo, Nano Lett. **13**, 2615 (2013).

[12] J. Hong et al., Nat. Commun. **6**, 6293 (2015).

[13] V. Carozo et al., Sci. Adv. **3**, e1602813 (2017).

[14] J. Suh et al., Nano Lett. **14**, 6976 (2014).

[15] J.-K. Huang, J. Pu, C.-L. Hsu, M.-H. Chiu, Z.-Y. Juang, Y.-H. Chang, W.-H. Chang, Y. Iwasa, T. Takenobu, and L.-J. Li, ACS Nano **8**, 923 (2014).

[16] M.-Y. Li et al., Science **349**, 524 (2015).

[17] W.-T. Hsu, Y.-L. Chen, C.-H. Chen, P.-S. Liu, T.-H. Hou, L.-J. Li, and W.-H. Chang, Nat. Commun. **6**, 8963 (2015).

[18] X. Song, S. Xie, K. Kang, J. Park, and V. Sih, Nano Lett. **16**, 5010 (2016).

[19] D. Kozawa et al., Nat. Commun. **5**, 4543 (2014).

[20] A. Srivastava, M. Sidler, A. V. Allain, D. S. Lembke, A. Kis, and A. Imamoğlu, Nat. Nanotechnol. **10**, 491 (2015).

[21] Y.-M. He et al., Nat. Nanotechnol. **10**, 497 (2015).

[22] M. Koperski, K. Nogajewski, A. Arora, V. Cherkez, P. Mallet, J.-Y. Veuillen, J. Marcus, P. Kossacki, and M. Potemski, Nat. Nanotechnol. **10**, 503 (2015).

[23] C. Chakraborty, L. Kinnischtzke, K. M. Goodfellow, R. Beams, and A. Nick Vamivakas, Nat. Nanotechnol. **10**, 507 (2015).

[24] See Supplemental Material at http://link.aps.org/supplemental/10.1103/PhysRevLett.119.046101 for sample growth, STM and STS, photoluminescence or Raman, and density functional theory calculations, which includes Refs. [25–30].

[25] S. Zhang, D. Huang, and S. Wu, Rev. Sci. Instrum. **87**, 063701 (2016).

[26] G. Kresse and D. Joubert, Phys. Rev. B **59**, 1758 (1999).

[27] G. Kresse and J. Furthmuller, Comput. Mater. Sci. **6**, 15 (1996).

[28] J. Klimes, D. R. Bowler, and A. Michaelides, J. Phys. Condens. Matter **22**, 022201 (2010).

[29] Z.-X. Hu, X. Kong, J. Qiao, B. Normand, and W. Ji, Nanoscale **8**, 2740 (2016).

[30] X.-X. Zhang, Y. You, S. Y. F. Zhao, and T. F. Heinz, Phys. Rev. Lett. **115**, 257403 (2015).

[31] H. Liu et al., Nat. Commun. **6**, 8180 (2015).

[32] M. Yankowitz, D. McKenzie, and B. J. LeRoy, Phys. Rev. Lett. **115**, 136803 (2015).

[33] Y. L. Huang *et al.*, Nano Lett. **16**, 3682 (2016).

[34] M. M. Ugeda *et al.*, Nat. Mater. **13**, 1091 (2014).

[35] Y. Wang, S. Zhang, D. Huang, J. Cheng, Y. Li, and S. Wu,
2D Mater. **4**, 015021 (2017).

[36] S. Barja *et al.*, Nat. Phys. **12**, 751 (2016).

[37] J. Cheng, T. Jiang, Q. Ji, Y. Zhang, Z. Li, Y. Shan, Y. Zhang,
X. Gong, W. Liu, and S. Wu, Adv. Mater. **27**, 4069 (2015).

[38] A. M. Jones *et al.*, Nat. Nanotechnol. **8**, 634 (2013).